RARE METALS

Thermal forming properties of a Cr-Mn-Si-Ni alloyed naval steel under different forming conditions by different constitutive models

Jia-Li Pang, Ze-Lin Zhu, Jing-Yu Zhang, Qiang Chen, Jie Zhou,
Yi Meng* , Sumio Sugiyama

Abstract A series of thermal compression tests on a Cr-Mn-Si-Ni alloyed naval steel were carried out at different strain rates (0.0005–0.0100 s^{-1}) at different temperatures (1023–1173 K). Based on the friction-corrected data obtained from the compression tests, strain-compensated Arrhenius-type constitutive (SCAC) and backpropagation artificial neural network (BP-ANN) models with the optimized structure of the Cr-Mn-Si-Ni alloyed naval steel were established. The optimized BP-ANN model, where the operation time and overfitting of BP-ANN were shortened and avoided, respectively, exhibited improved predictive performance. The two models were assessed further in terms of the correlation coefficient (R), average absolute relative error, and root mean square error. The results validated that the optimized BP-ANN model predicted the flow behavior of the Cr-Mn-Si-Ni alloyed naval steel better than the SCAC model. The effect of the forming temperature and strain rate on the microstructural evolution behavior of the naval steel during thermoplastic deformation was investigated through the electron backscatter diffraction analysis of the compressed samples. It was observed that the dynamic recrystallization of the naval steel was promoted by an increase in the forming temperature and a decrease in the strain rate during thermoplastic deformation.

Keywords Naval steel; Thermal compression; Recrystallization; Constitutive model

1 Introduction

Naval steels used in marine and offshore engineering manufacturing are required to exhibit high strength, excellent low-temperature impact toughness, and good weldability. To improve the low-temperature impact toughness while maintaining other mechanical properties, several types of alloyed naval steels have been designed and developed, including Cr-Mn-Si-Ni alloyed naval steel [1–4]. Thermoplastic deformation of metallic materials is a vital step to manufacture structural components from Cr-Mn-Si-Ni alloyed naval steel billets. The performance of structural components and the reliability of the entire marine product are determined by the thermal forming properties of naval steels under particular forming conditions [5, 6]. Therefore, it is necessary to investigate the thermal forming behavior of Cr-Mn-Si-Ni alloyed naval steels under different conditions, which has rarely been reported. In the past decades, a considerable number of research articles on the thermal deformation behavior of steels and alloys have been published. Shahriari et al. [7] studied the kinetics of the dynamic recrystallization (DRX) of BA-160 steel during thermal compression and compared it with a hypothetical dynamic recovery curve. Abed [8] proposed a microstructures-based constitutive relation to describe the plastic behavior of the DH-63 naval structural steel over a broad range of temperatures and strain rates.

J.-L. Pang, Z.-L. Zhu, J.-Y. Zhang, J. Zhou, Y. Meng*
College of Materials Science and Engineering, Chongqing
University, Chongqing 400044, China
e-mail: mengyi@cqu.edu.cn

Q. Chen
Southwest Technology and Engineering Research Institute,
Chongqing 400039, China

S. Sugiyama
Institute of Industrial Science, The University of Tokyo, Tokyo
153-8505, Japan

Dandekar et al. [9] investigated the flow behavior of Fe-21Cr-1.5Ni-5Mn alloy using thermal compression tests and established a strain rate sensitivity map.

Recently, computers have played an increasingly crucial role in the numerical simulation and analysis of the thermal forming processes of metallic materials. Based on the simulation results, suitable thermal forming parameters can be determined and optimized [10–12]. Consequently, a credible constitutive model that can accurately describe the mathematical relationship between the thermal forming properties such as the flow stress, and process parameters such as forming temperature, strain, and strain rate of metallic materials during the thermal forming process, must be embedded in the commercial numerical analysis software [13–15]. Therefore, it is essential to establish a suitable constitutive model for simulating the forming process of Cr-Mn-Si-Ni alloyed naval steel. Generally, the proposed constitutive models can be classified as phenomenological models, physics-based models, and artificial neural networks (ANNs) [16–20]. For phenomenological models, a detailed understanding of the physical phenomena involved in the thermoplastic deformation process is not required. In contrast, the constitutive relationship between the flow stress and forming temperature, strain rate, and strain can be determined through regression analysis. The most well-known and widely adopted phenomenological models include the Johnson–Cook constitutive model, hyperbolic Arrhenius-type constitutive model, and strain-compensated Arrhenius-type constitutive (SCAC) model. However, regression analysis inevitably reduces their accuracy in predicting the flow stress. Physics-based models include the Zerilli-Armstrong (ZA) [21] and the dynamic recrystallization (DRX) models [22], which consider thermoplastic deformation mechanisms such as dislocation and thermal activation kinetics. However, their application in numerical simulations is limited by the difficulty in determining the parameters of metallic materials and the complexity of physical models. ANNs, especially backpropagation artificial neural networks (BP-ANN), show better prediction performance than the above-mentioned models; thus, they have been gradually used in the numerical simulations of the thermal forming processes of metallic materials [23–26]. In addition, various novel constitutive models have been proposed for several decades. For instance, Maati et al. [27] developed a statistical and physically based model for predicting the elastic return in a sheet after a bending operation, and the hybrid model was successfully utilized in numerical simulations. Oliveira et al. [28] introduced a novel three-dimensional constitutive model that describes the thermomechanical behavior of shape memory alloys. Ashrafian and Kordkheili [29] proposed a viscoplastic temperature-dependent constitutive model, which was proven to possess the best predictivity by comparison of Ti-6Al-4V at high-temperature conditions under quasi-static rates.

Recently, ANNs have received considerable attention and have been optimized in previous reports. For example, nested functions outside ANN have been developed to improve their accuracy. An improved BP-ANN algorithm based on a genetic algorithm was proposed by Huang et al. [30] to predict the thermoplastic deformation behavior of an aluminum alloy. Based on particle swarm optimization, Wan et al. [31] optimized a double-hidden layer neural network to predict the flow stress of zirconium alloys under different thermal forming conditions. To obtain the optimal random weights and biases of BP-ANN, an optimization program with constrained nonlinear functions was established by Murugesan et al. [32]. All of these constitutive models successfully improved the learning capacity and prediction accuracy of the ANN through complicated functions. Nevertheless, little research has been done on the optimization of the BP-ANN structure.

In this study, a series of isothermal compression tests were performed to investigate the thermoplastic deformation behavior of a Fe-0.16C-0.18Si-0.02Cr-1.45Mn-0.005Ni alloyed naval steel. Using BP-ANN and SCAC models, the accurate prediction of the flow stress of the naval steel under different forming conditions, such as forming temperature, strain rate, and strain, was performed. To enhance the predictability to the furthest extent, attempts to determine the best settings for BP-ANN were performed through a series of experiments and analyses. The results can provide guidance for establishing excellent BP-ANN models for the thermoplastic deformation behaviors of other metallic materials. Moreover, a comparative study on the prediction accuracy between the optimized BP-ANN and SCAC models was conducted based on the correlation coefficient (R), average absolute relative error (AARE) and root mean square error (RMSE). Additionally, the influence of friction on the thermal compression experimental results was not negligible, as shown by the effect of the uncorrected data on the accuracy of the constitutive equation and the reliability of finite element simulations [33, 34]. Hence, the raw data obtained from the thermal compression experiments must be corrected prior to the numerical analysis. Eventually, the microstructural evolution behaviors of Cr-Mn-Si-Ni alloyed naval steel under various thermal forming conditions were studied through scanning electron microscopy (SEM) and electron backscatter diffraction (EBSD). Finally, a processing map and strain rate sensitivity map were developed to optimize the thermal deformation parameters and control the microstructural evolution.

2 Experimental

Cr-Mn-Si-Ni alloyed naval steel was used as the experimental material. Table 1 summarizes its chemical composition. The original naval steel was modeled into cylindrical samples with dimensions of $\Phi 8$ mm $\times$ 12 mm. Thermal compression tests on the cylindrical samples were conducted using a thermomechanical simulator (Gleeble-3500, USA) according to the experimental procedures illustrated in Fig. 1. First, the cylindrical samples were heated to 1223 K at a heating rate of 20 K·s^{-1} and held isothermally for 180 s. Subsequently, the reheated samples were cooled to different forming temperatures (1023, 1073, 1123 and 1173 K) at a cooling rate of 5 K·s^{-1}. After the isothermal holding at the forming temperature for 30 s, the samples were compressed to a true strain of 0.7 with different strain rates (0.0005, 0.0010, 0.0050 and 0.0100 s^{-1}). The load-stroke data during the compression tests were recorded by a computer system. The compressed samples were immediately cooled to room temperature using cold water.

For the microstructural examination, the compressed specimens produced using different forming parameters were cut parallel to the compression direction. An EBSD instrument (NordlysMax2, Britain) installed in an SEM (JEOL JSM-7800F, Japan) was used to examine the microstructure and obtain information about DRX. The scanning step size used was 0.5 μm. SEM was employed to observe the microstructures. Subsequently, EBSD results were analyzed using HKL Channel 5 software. In this analysis, grain orientation spreads of 1° and 2° were selected as the threshold values to distinguish the recrystallized grains, substructured, and deformed grains. The grains with orientation spread lower than 1° were identified as recrystallized grains and are represented in blue, those with grain orientation spread values between 1° and 2° were identified as substructured grains and are represented in yellow, and the grains with values higher than 2° were referred to as deformed grains and are represented in red. In addition, low-angle grain boundaries (LAGBs, grain boundary misorientation lower than 15°) and high-angle grain boundaries (HAGBs, grain boundary misorientation higher than 15°) are represented by grey lines and black

lines, respectively. Furthermore, the phases were distinguished by the band slope of grains in this software (ferrite: band slope higher than 130; bainite: band slope higher than 75 but lower than 130; martensite: band slope lower than 75).

3 Results and discussion

3.1 Correction of friction effect

The friction between the specimen and dies could not be eliminated completely, although a lubricant was used during the thermal compression tests. Because friction restricted the movement in the radial direction of the material at both ends of the specimen, the compressed specimen exhibited a drum-like shape. To obtain more accurate true stress-true strain curves, the original flow stress must be friction-corrected [35]. Equation (1) is often employed to calculate the true stress by eliminating the effect of friction between the specimen and the dies [36, 37]. From Eqs. (2–5), a constant friction coefficient evaluation formula for the cylindrical specimen was proposed in previous reports on the energy method [38, 39]:

$$\sigma = \frac{\sigma_e}{1 + (2/3\sqrt{3})m\left(\frac{R_0}{H_0 \exp(3\varepsilon/2)}\right)} \tag{1}$$

$$m = \frac{(R/H)b}{(4/\sqrt{3}) - (2b/3\sqrt{3})} \tag{2}$$

$$b = 4\frac{R_M - R_T}{R}\frac{H}{H_0 - H} \tag{3}$$

$$R = R_0\sqrt{\frac{H_0}{H}} \tag{4}$$

$$R_T = \sqrt{3\frac{H_0}{H}R_0^2 - 2R_M^2} \tag{5}$$

where σ is the corrected flow stress, σ_e is the experimentally measured flow stress, ε is the strain, m is the constant friction coefficient, and b is the barrel parameter. As shown in Fig. 1, R_0 and H_0 are the initial radius and height of the specimen before deformation, respectively; R and H are the final average radius and height of the compressed specimen, respectively; whereas R_M and R_T are the maximum and top radii of the compressed specimen, respectively. Figure 2 shows a comparison between the original and the friction-corrected flow stress curves of the steel samples compressed under various conditions.

Table 1 Chemical composition of naval steel (wt%)

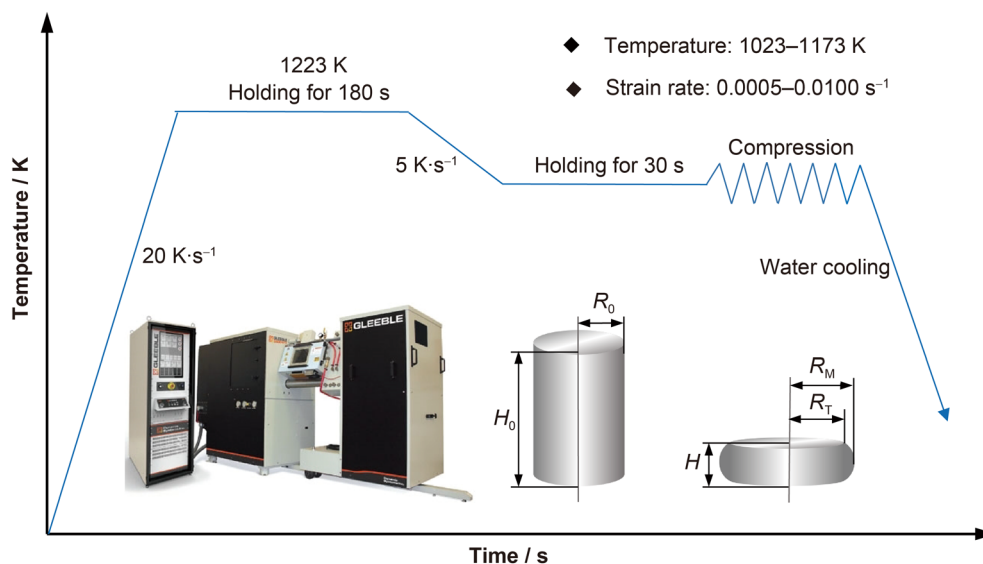| C	Si	Mn	Ni	Cr	Fe
0.161	0.184	1.452	0.005	0.019	Bal.

Fig. 1 Schematic illustration of thermal compression test procedure and resulting geometric change in cylindrical samples
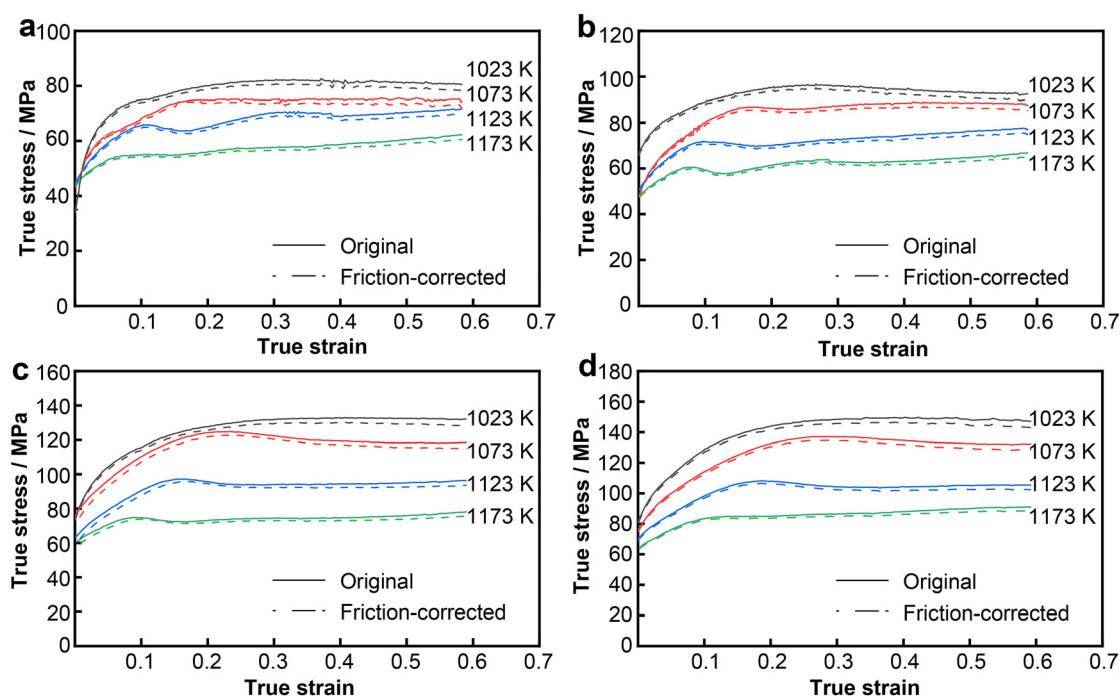

Fig. 2 Original and friction-corrected flow stress curves of naval steel samples compressed at strain rates of **a** 0.0005 s^{-1}, **b** 0.0010 s^{-1}, **c** 0.0050 s^{-1}, and **d** 0.0100 s^{-1}

3.2 Thermal rheological behaviors of Cr-Mn-Si-Ni alloyed naval steel

The true stress of Cr-Mn-Si-Ni alloyed naval steel during thermal compression was affected by the forming temperature (T), strain rate ($\dot{\varepsilon}$), and true strain (ε) (Fig. 2). In the early stages of thermal compression, the rheological stress value increased with the increase in the true strain. This is possibly due to the rapid increase in the dislocation density

in the compressed naval steel. These dislocations tangled with each other and resulted in the increase in the dislocation motion resistance. Gradually, the hardening rate became higher than the softening rate of the naval steel and subsequently caused work hardening. Once the dislocation density in the naval steel accumulated to a certain extent, the microstructural evolution behavior, such as dynamic recovery (DRV) and DRX, with the softening effect in the material progressively increased. Thus, the softening and

hardening effects inside the naval steel achieved a dynamic balance [40, 41]. This resulted in good stability of the true stress of the Cr-Mn-Si-Ni alloyed naval steel as the thermal compression continued.

3.3 Arrhenius-type constitutive equation

In the Arrhenius-type constitutive model, the Zener-Hollomon parameter (Z) expressed in Eq. (6) was employed to represent the influences of deformation temperature and strain rate on the thermoplastic deformation properties of the naval steel:

$$Z = \dot{\varepsilon}\exp(Q/RT) \tag{6}$$

In this Arrhenius-type constitutive equation, the flow stress is expressed in terms of the widely accepted hyperbolic law, as shown in Eq. (7).

$$\dot{\varepsilon} = \begin{cases} A_1\sigma^{n_1}\exp(-Q/RT) & (\alpha\sigma < 0.8) \\ A_2\exp(\beta\sigma)\exp(-Q/RT) & (\alpha\sigma > 1.2) \\ A[\sinh(\alpha\sigma)]^n\exp(-Q/RT) & (\text{for all } \sigma) \end{cases} \tag{7}$$

where Q is the apparent activation energy of thermoplastic deformation, R is the ideal gas constant equal to 8.314 J·(mol·K)$^{-1}$, and A_1, A_2, A, α, b, β, n and n_1 are the material constants. The value of α was calculated using $\alpha = b/n_1$. The natural logarithms of both sides of Eq. (7) were converted into Eqs. (8–10):

$$\ln\dot{\varepsilon} = \ln A_1 + n_1\ln\sigma - Q/RT \quad (\alpha\sigma < 0.8) \tag{8}$$

$$\ln\dot{\varepsilon} = \ln A_2 + \beta\sigma - Q/RT \quad (\alpha\sigma > 1.2) \tag{9}$$

$$\ln\dot{\varepsilon} = \ln A + n\ln[\sinh(\alpha\sigma)] - Q/RT \quad (\text{for all } \sigma) \tag{10}$$

As shown in the equations above, the traditional Arrhenius constitutive equation was developed without considering the effect of the true strain on the flow stress. To obtain a more accurate constitutive equation for this steel, the impact of the true strain when calculating the material parameters was considered. The parameters α, N, A and Q can be expressed as a function of the sixth-degree polynomial of the true strain. Correspondingly, the corresponding material constants were calculated every 0.05 in the range of true strain from 0.05 to 0.60 by the linear fitting method. Thus, the accuracy of the SCAC model can be improved. For example, the material constants under the true strain $\varepsilon = 0.5$ were calculated. As shown in Eq. (8), the relationship between $\ln\dot{\varepsilon}$, $\ln\sigma$, and σ at a constant forming temperature is linear. As shown in Fig. 3a, b, the values of the average slopes n_1 and β at different forming temperatures were calculated as 6.3171 and 0.07268, respectively.

According to Eq. (8), $\ln\dot{\varepsilon}$–$\ln[\sinh(\alpha\sigma)]$ is plotted in Fig. 3c. The average slope was calculated to be 4.785 using linear regression analysis. According to Fig. 3d and

Eq. (8), $\ln\sinh(\alpha\sigma)$ has a linear relationship with the forming temperature once compression tests are conducted with a constant strain rate. Based on the data obtained from Fig. 3c, d, the thermoplastic deformation activation energy of this steel was calculated to be 188.398 kJ·mol^{-1}. To calculate the value of parameter A, Q was assumed to be constant at different forming temperatures. When the strain rate is constant, the plot of $\ln Z$–$\ln\sinh(\alpha\sigma)$ can be obtained from the intercept of the fitting line. The value of parameter A was 8.68×10^5 from the linear regression analysis, as shown in Fig. 3e. Subsequently, the material constants obtained under different strain conditions were used to fit the sixth-order polynomial. The relationship between the material constants α, N, A, Q and ε can be expressed by the polynomial Eq. (11), whose coefficients are listed in Table 2.

$$\begin{cases} \alpha = B_0 + B_1\varepsilon + B_2\varepsilon^2 + B_3\varepsilon^3 + B_4\varepsilon^4 + B_5\varepsilon^5 + B_6\varepsilon^6 \\ n = C_0 + C_1\varepsilon + C_2\varepsilon^2 + C_3\varepsilon^3 + C_4\varepsilon^4 + C_5\varepsilon^5 + C_6\varepsilon^6 \\ Q = D_0 + D_1\varepsilon + D_2\varepsilon^2 + D_3\varepsilon^3 + D_4\varepsilon^4 + D_5\varepsilon^5 + D_6\varepsilon^6 \\ \ln A = E_0 + E_1\varepsilon + E_2\varepsilon^2 + E_3\varepsilon^3 + E_4\varepsilon^4 + E_5\varepsilon^5 + E_6\varepsilon^6 \end{cases} \tag{11}$$

The experimental and predicted flow stress curves are shown in Fig. 4. It can be seen that the SCAC model can show the flow stress variation trend of the naval steel in the thermal deformation process. However, there is an evident deviation between the predicted and the actual values under different forming conditions.

3.4 Establishment and optimization of BP-ANN model

ANN is a complicated network system of information processing and nonlinear transformation that is connected by multiple neurons. It is capable of self-learning by simulating in a similar way as the human brain processes information. BP-ANN is one of the most mature and extensive networks. The typical BP-ANN model consists of the input, hidden, and output layers. In this study, T, $\dot{\varepsilon}$, and ε are the three columns of input data, while the corrected σ is the output data. After inputting all data into the network, the data of neurons in the upper layer were multiplied by the initial weight, and then were transmitted to the neurons in the next layer. By calculating and comparing the error between the predicted result and the experimental data, forward feedback was provided, and the weight was then adjusted until the error declined to the set value. Eventually, after learning and training, ANN has a high prediction accuracy for nonlinear relationship [42–44]. The settings of BP-ANN, which include the number of hidden layers, neurons in each layer, the activation function, and the selection of the training algorithm in each layer, have certain influences on the
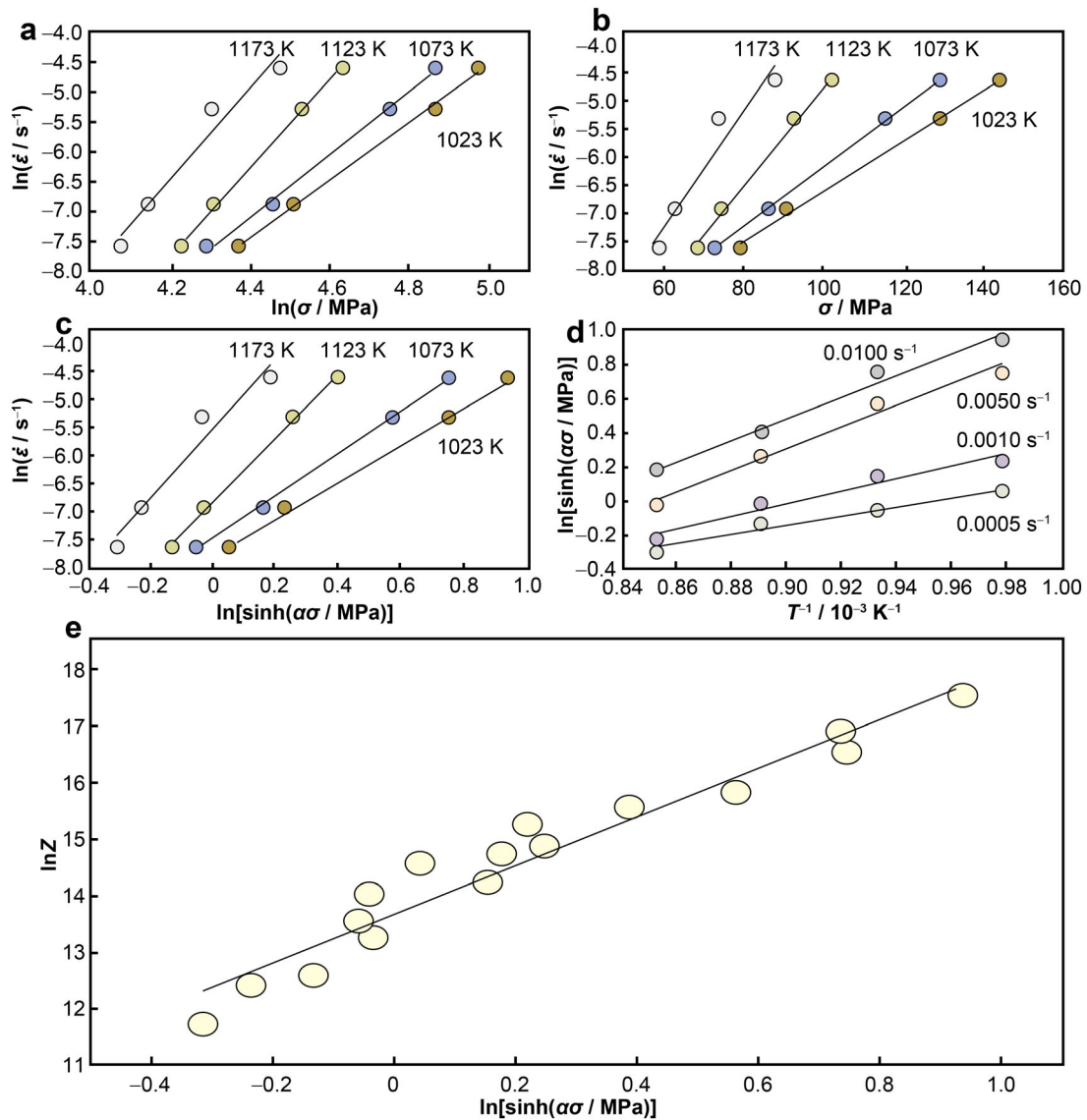
Fig. 3 Solving process diagrams of material parameters **a** n_1, **b** β, **c** n, **d** Q, and **e** A of naval steel

Table 2 Coefficients of polynomial data of naval steel used in Eq. (11)

B_i	C_i	D_i	E_i
0.01680	5.96891	174,653.5	11.72
− 0.08836	− 7.72253	− 264,941.0	− 22.71
0.64614	− 144.43300	2,706,667.0	277.10
− 2.50079	1401.95860	− 13,248,300.0	− 451.10
5.30975	− 4625.49700	− 13,248,300.0	− 1011.30
− 5.83873	6644.92110	34,656,900.0	3008.11
2.59647	− 3525.36800	− 21,962,800.0	− 1940.90

prediction accuracy and calculation time of the neural network.

A multi-hidden layer neural network has a strong generalization capability and high prediction accuracy; however, the training time is relatively long. The number of neurons in the hidden layer has a significant impact on prediction accuracy of the neural network. If there are too few neurons, the network cannot learn well, and the accuracy of the training is affected. However, with too many neurons, the training time increases considerably, and the network tends to overfit [32]. The activation function is adopted to add nonlinear elements to improve the expression ability of the neural network for the model and resolve the problems encountered using the linear model. In this study, the tansig function with a fast convergence speed and high applicability was selected. Equation (12) expresses the tansig function. For the output layer, the activation function purelin (linear function) was directly selected. The problem was assumed to be linear at the output layer because the output was proportional to the weighted total input.
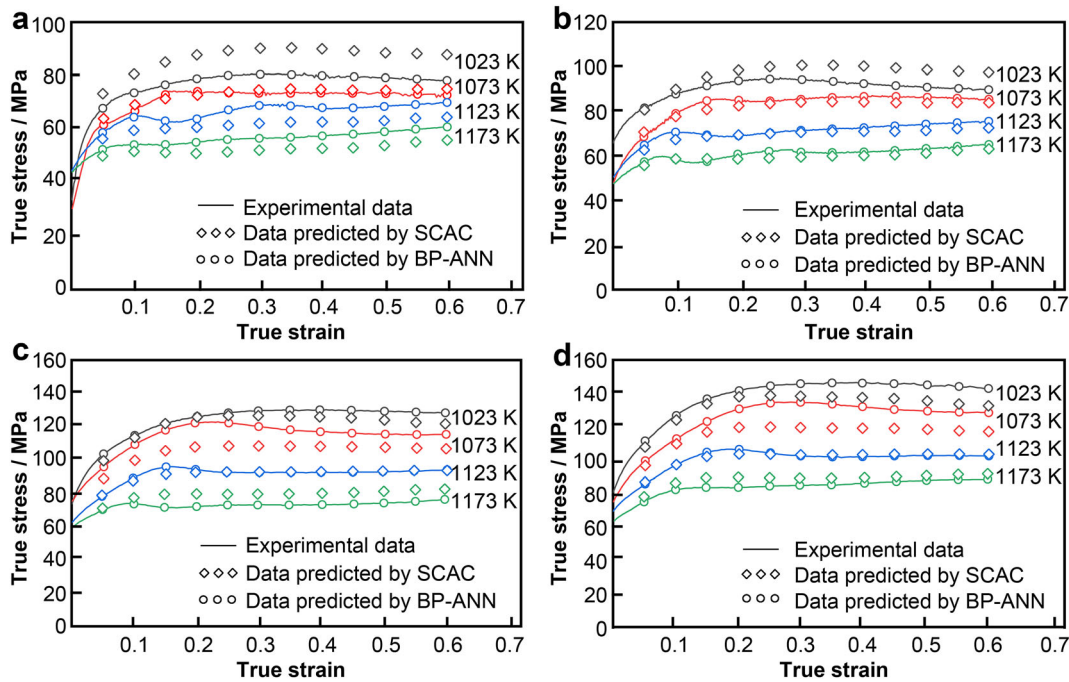
Fig. 4 Experimental flow stress curves of naval steel and curves predicted by SCAC model and BP-ANN model at strain rates of **a** 0.0005 s^{-1}, **b** 0.0010 s^{-1}, **c** 0.0050 s^{-1}, and **d** 0.0100 s^{-1}

$$f(x) = \tanh(x) = \frac{e^x - e^{-x}}{e^x + e^{-x}} \qquad (12)$$

In addition, among the commonly used training functions, the trainlm (Levenberg–Marquardt) function is the fastest backpropagation algorithm; however, it requires more computer memory. The trainbr (Bayesian regularization) is a network training function that updates the weight and bias values according to the Levenberg–Marquardt optimization. It minimizes a combination of squared errors and weights and then determines the correct combination to develop a network with better generalization [45, 46]. To optimize BP-ANN, the effects of the number of hidden layers, number of hidden layer neurons, and training algorithm on the learning ability of ANN were evaluated.

The BP-ANN structure of the double hidden layers for flow stress prediction is shown in Fig. 5. The values of R (Eq. (13)), AARE (Eq. (14)), and RMSE (Eq. (15)) were used to evaluate the learning capability and prediction accuracy of the ANN [47]:

$$R = \frac{\sum_{i=1}^{N} (\sigma_E - \overline{\sigma_E})(\sigma_P - \overline{\sigma_P})}{\sqrt{\sum_{i=1}^{N} (\sigma_E - \overline{\sigma_E})^2 \sum_{i=1}^{N} (\sigma_P - \overline{\sigma_P})^2}} \qquad (13)$$

$$\text{AARE} = \frac{1}{N} \sum_{i=1}^{N} \left| \frac{\sigma_E - \sigma_P}{\sigma_E} \right| \times 100\% \qquad (14)$$

$$\text{RMSE} = \sqrt{\frac{1}{N} \sum_{i=1}^{N} (\sigma_E - \sigma_P)^2} \qquad (15)$$

where σ_E is the experimental data, σ_P is the predicted value of the phenomenological model, $\overline{\sigma_E}$ and $\overline{\sigma_P}$ are the mean values of σ_e and σ_p, respectively, and N is the number of data points used in the survey. R is usually used to assess the linear relationship between the predicted and experimental observation values; nevertheless, an R value closer to 1 does not imply that the predicted value is in good agreement with the experimental value to some extent. This is because the value of R may be easily influenced by extremely high or low values. Therefore, AARE and RMSE are used to test the reliability of the model [9, 48]. These statistical parameters can be utilized to check the predictability of the established constitutive model by comparing the relative error of the prediction with the actual value of the variable [49, 50]. Because the reliability of BP-ANN depends strongly on the quantity of high-quality experimental data and characteristic variables, 960 discrete data points were selected from 16 stress–strain curves (Fig. 2) of Cr-Mn-Si-Ni alloyed naval steel ranging from 0.01 to 0.60 with an interval of 0.01. Among these data sets, 767 data points were randomly chosen to train the artificial neural network, while 193 data points were utilized to test the performance of the ANN
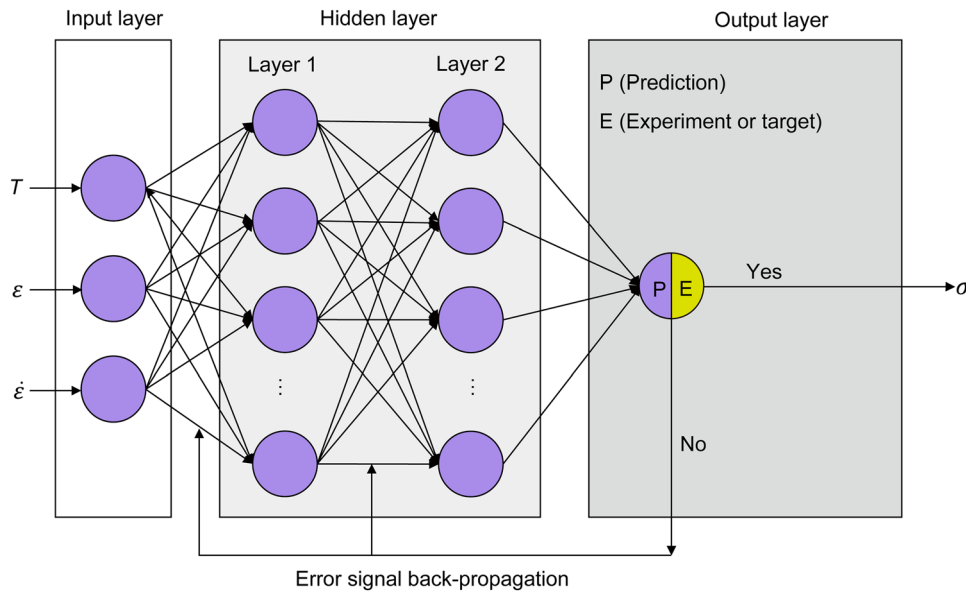
Fig. 5 BP-ANN structure diagram for flow stress prediction of double hidden layers

Table 3 Setting of BP-ANN for prediction of flow stress with double hidden layers

Parameters	Values
Number of training samples	767
Number of test samples	193
Number of hidden layers	1 or 2
Hide layer activation functions	Tansig
The output layer activates the function	Purelin
The training function	Trainlm or trainbr
Learning function	Learngdm
Number of variables in the input layer	3 (three variables)
Number of variables in the output layer	1 (one variable)
Learning rate	0.01
Number of cells per hidden layer	4–50 neurons
The accuracy to be trained	1×10^{-5}

model. The other settings of the BP-ANN model in this study are listed in Table 3.

Moreover, the entire input and output variables must be normalized before training the network. Equation (16) is widely adopted to accomplish this process to obtain a usable form for the ANN model [51]:

$$X_N = \frac{X - 0.95X_{\min}}{1.05X_{\max} - 0.95X_{\min}} \tag{16}$$

where X is the measured experimental data (including the values of σ, $\dot{\varepsilon}$, ε, and T), $X_{\min}$ and $X_{\max}$ are the minimum and maximum values of the chosen actual data,

respectively, and X_N represents the modified data after normalization.

Figure 6a, c, e illustrates the performance of the single-hidden layer neural network with different numbers of neurons and training functions, while Fig. 6b, d, f shows the performance of the double-hidden layer neural network with different numbers of neurons selected. For both hidden layers, trainbr was selected as the training function. With an increase in the number of neurons, the prediction accuracy of both the single-hidden and the double-layer neural network initially increases rapidly. However, the prediction accuracy when the number of weights (W) of the neural network reached approximately 112 was the highest; it remained stable even with an increase in the number of neurons. W is expressed as:

$$W = iH_1 + \sum_{1}^{N} H_i H_{i+1} + H_N O \tag{17}$$

where i and O are the numbers of neurons in the input and output layers, respectively, H_i is the number of neurons in the hidden layer of layer i, and N is the number of data used in this survey.

The performance of the ANN model was evaluated at each setting. As shown in Fig. 6, the R value between the experimental value of the flow stress and the predicted value from the BP-ANN model in single and double hidden layers (with the trainbr as the training function) was stable from 0.99996 to 0.99998. Meanwhile, AARE and RMSE remained stable at 0.17%–0.19% and 0.20–0.23, respectively. From these figures, it can be seen that the
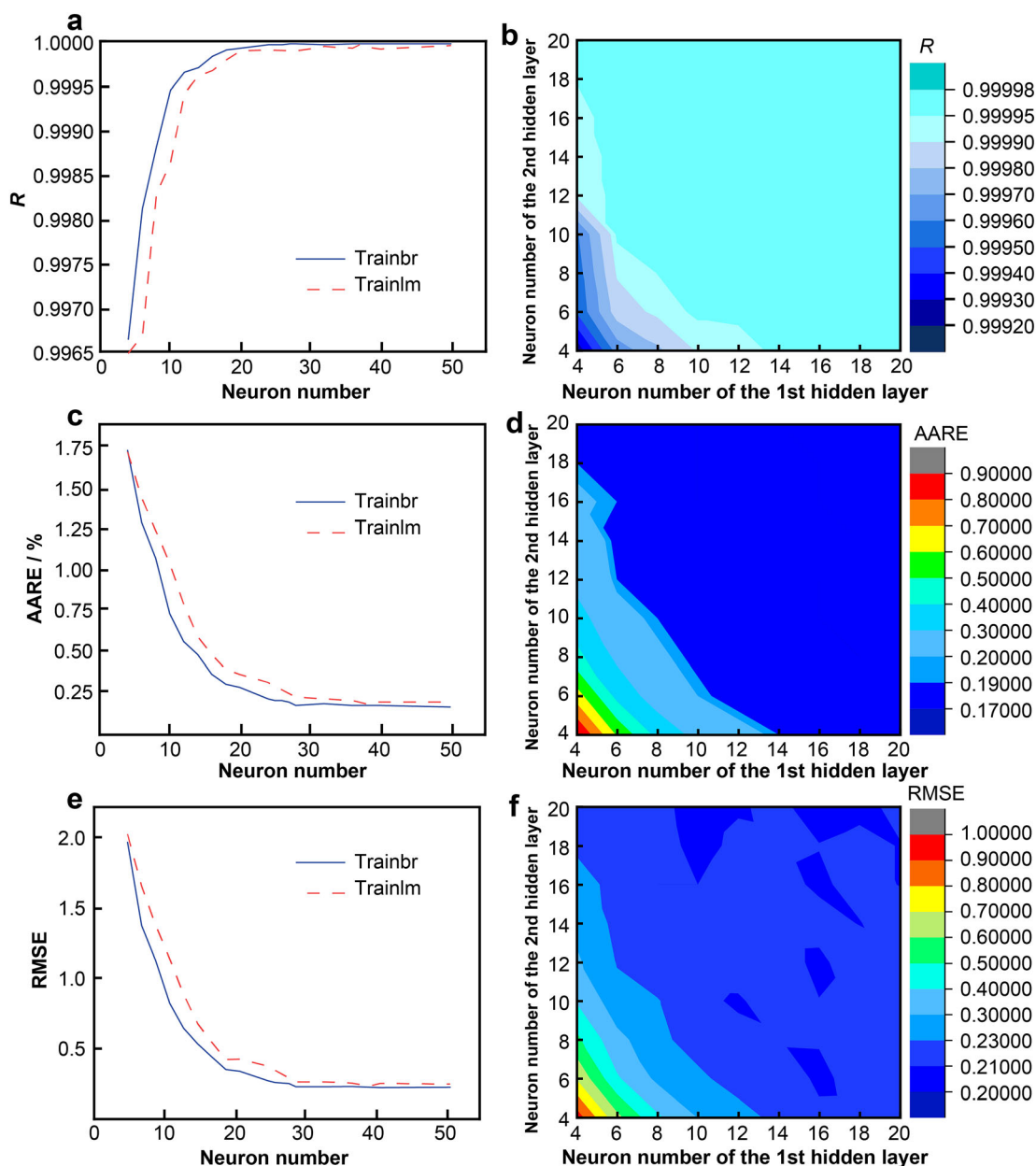
Fig. 6 Relationship between prediction accuracy of BP-ANN and training function, number of hidden layers and number of neurons in hidden layers: **a** and **b** R, **c** and **d** average absolute relative error (AARE), and **e** and **f** root mean square error (RMSE)

usage of more hidden layers in the BP-ANN model does not necessarily result in the better predictability of the flow stress. In addition, Fig. 6a, c, e reveals that the BP-ANN operated more accurately when the trainbr training function was used rather than the trainlm function. Thus, for the precise and accurate prediction of flow stress, a single hidden layer BP-ANN using the trainbr training function was selected, and the number of neurons in the hidden layer was set to 28. In this case, an ANN model that

showed the best performance in a relatively short operation time was realized.

The experimentally measured flow stress curves of the naval steel and those predicted by the optimized BP-ANN model are also presented in Fig. 4. The predicted flow stress curves highly coincide with the experimental curves. Meanwhile, the hardening and softening regions of this naval steel during thermal deformation can be identified from the predicted results. Accordingly, the optimized BP-ANN
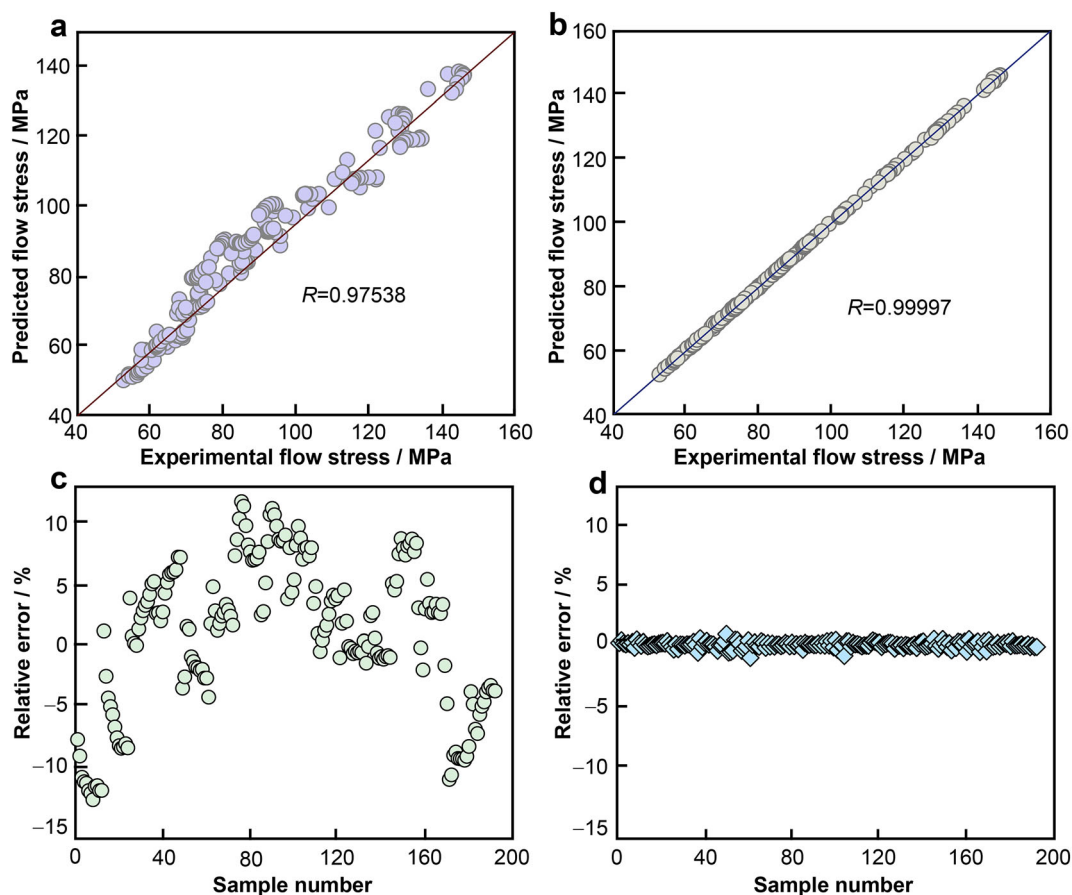
Fig. 7 Correlation between experimental and predicted flow stress values by **a** SCAC and **b** optimized BP-ANN models; relative errors between experimental and predicted flow stress values by **c** SCAC and **d** optimized BP-ANN models

model can be adopted to simulate the thermal deformation behavior of the Cr-Mn-Si-Ni alloyed naval steel.

3.5 Comparison between SCAC and BP-ANN models

The accuracy and predictability of the SCAC and BP-ANN models were examined and compared using the values of R, AARE, and RMSE. The correlations between the experimental and the predicted data from the SCAC and optimized BP-ANN models are illustrated in Fig. 7a, b, respectively. Although most data points obtained by the two models were distributed close to the line, the optimized BP-ANN exhibited better performance. For an instance, the R value for the SCAC and the optimized BP-ANN models was 0.97538 and 0.99997, respectively. This indicates that the flow stress predicted by the optimized BP-ANN model has a better correlation with the experimental data.

The predictabilities of the SCAC and optimized BP-ANN models in terms of the flow stress of the Cr-Mn-Si-Ni alloyed naval steel during the thermal deformation process are summarized in Table 4. Similarly, according to the

Table 4 Calculated values of R, AARE, and RMSE for two models

Model	R	AARE / %	RMSE / MPa
SCAC	0.97538	5.11	5.81
Optimized BP-ANN	0.99997	0.17	0.42

calculated values of R, AARE, and RMSE, the optimized BP-ANN model rendered a remarkably better predicted result than the SCAC model. Owing to its excellent accuracy and reliability, the optimized BP-ANN model can be used to predict the thermal deformation behavior of the alloyed naval steel. Furthermore, the capabilities of these two models were analyzed using the relative error. The relative error is defined by Eq. (18) [18]:

$$\text{Relative error} = \left(\frac{\sigma_E - \sigma_P}{\sigma_E} \right) \times 100\% \tag{18}$$

The relative errors between the experimental results and the flow stress predicted by the SCAC and optimized BP-ANN models in the entire true strain range are shown

graphically in Fig. 7d, respectively. The relative errors obtained from SCAC model ranged between − 15% and 12%, whereas those calculated from the optimized BP-ANN model were almost close to zero (from − 1.2% to 0.8%). This result further proved that the optimized BP-ANN model has a surprisingly high predictive performance for the flow stress of this naval steel during thermal forming.

The results discussed above demonstrate that the optimized BP-ANN model exhibited a better performance than the SCAC model in predicting the thermal forming behavior of Cr-Mn-Si-Ni alloyed naval steel. Furthermore, this implies that the optimized BP-ANN model can possibly be used to conduct a numerical simulation of the thermoplastic deformation of this steel to obtain more accurate results.

3.6 Microstructural evolution

SEM images of the Cr-Mn-Si-Ni alloyed naval steel samples compressed under various conditions are presented in Fig. 8. Although the austenite in the compressed samples transformed into martensite after water cooling, the original austenite grain boundaries could still be seen based on the direction of the martensite lath. The grains in the compressed samples were equiaxed, which demonstrates that DRX occurred. The occurrence of DRX can also be proven by the existence of peak stress on the flow stress curves (Fig. 2). Moreover, because the carbon content of the naval steel was only 0.16 wt%, only a small number of carbides precipitated; thus, carbides were not visible in SEM micrographs.

The inverse pole maps obtained from EBSD analysis of the Cr-Mn-Si-Ni alloyed naval steel samples compressed

under different conditions are illustrated in Fig. 9. The corresponding average equivalent circle diameters are listed in Table 5. On the other hand, the grain orientation spread maps of the samples are presented in Fig. 10. From these figures, it can be seen that the compressed naval steel samples were dominated by recrystallized grains. The volume fraction of grains and the number fraction of the misorientation angle in the naval steel samples are also shown in Fig. 10.

As shown in Fig. 8a, c, e, the grain size decreased with strain rate increasing when the samples were compressed at 1023 K. Statistical analysis results obtained from EBSD analysis data presented in Table 5 further confirmed the effect of strain rate on the equivalent circle diameter in the deformed samples. When the strain rate was increased from 0.0005 to 0.0100 s^{-1}, the equivalent circle diameter of the specimen compressed at 1023 K decreased from 5.57 to 3.57 μm. At the same time, the grain size increased with forming temperature increasing. As shown in Table 5, the grain size increased from 3.57 to 7.37 μm as the forming temperature was increased from 1023 to 1173 K. Moreover, the volume fraction of the recrystallized grains in the specimen compressed at 1023 K increased with strain rate decreasing, as shown in Figs. 9 and 10a. Equiaxed grains dominated the microstructure of the naval steel samples compressed at a strain rate of 0.0100 s^{-1} because of the insufficient time for the growth of the recrystallized grains. The recrystallized grain size increased when the strain rate decreased from 0.0100 to 0.0005 s^{-1}, as shown in Fig. 10. When the strain rate increased from 0.0005 to 0.0100 s^{-1}, the volume fraction of the LAGBs increased from 24.8% to 35.2%. The increased fraction of LAGBs with strain rate
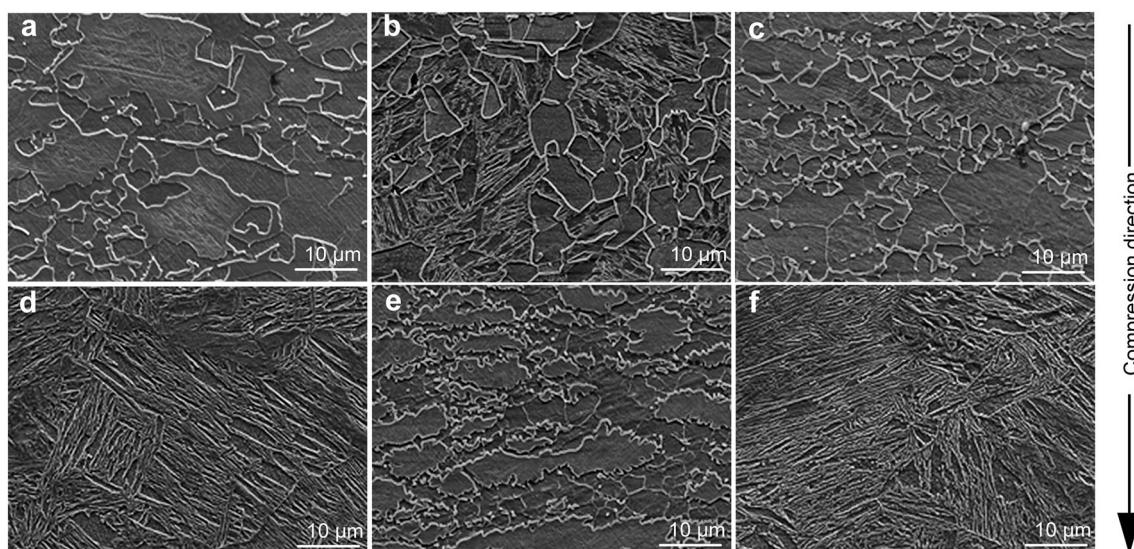

Fig. 8 SEM images of naval steel samples compressed under various conditions: **a** 1023 K, 0.0005 s^{-1}; **b** 1073 K, 0.0005 s^{-1}; **c** 1023 K, 0.005 s^{-1}; **d** 1123 K, 0.0005 s^{-1}; **e** 1023 K, 0.0100 s^{-1}; **f** 1173 K, 0.0005 s^{-1}
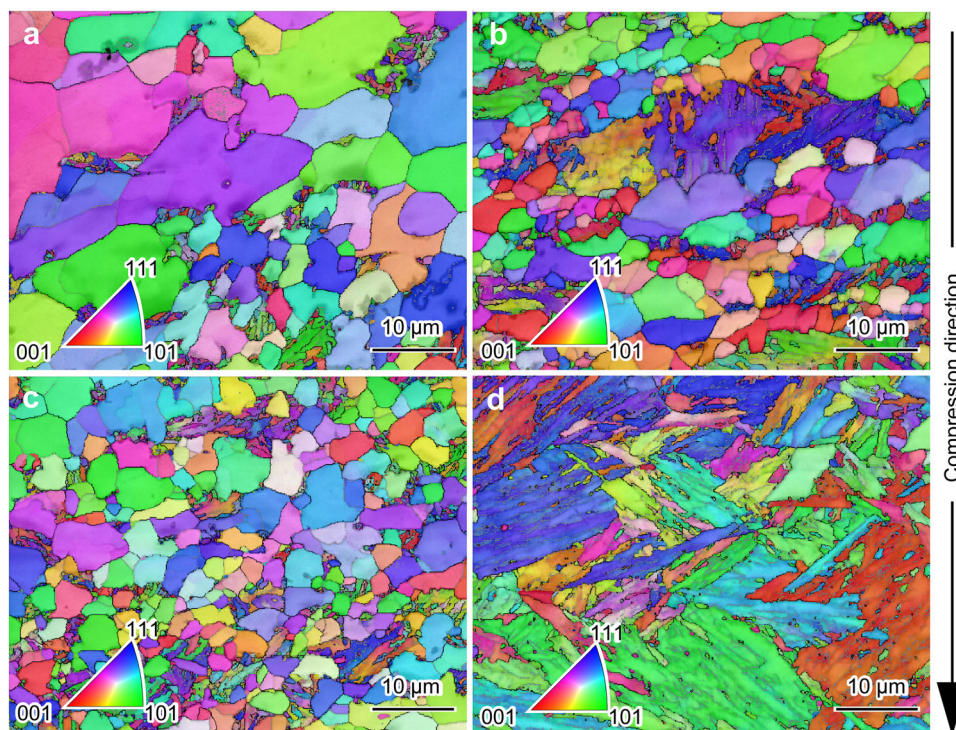
Fig. 9 Inverse pole maps of naval steel samples compressed under various experimental conditions: **a** 1023 K, 0.0005 s^{-1}; **b** 1023 K, 0.0050 s^{-1}; **c** 1023 K, 0.0100 s^{-1}; **d** 1173 K, 0.0100 s^{-1}

Table 5 Equivalent circle diameter of naval steel samples compressed under various conditions

Forming temperature / K	Strain rate / s^{-1}	Equivalent circle diameter / μm
1023	0.0005	5.57
1023	0.0050	3.82
1023	0.0100	3.57
1173	0.0100	7.37

increasing was due to the limited time for the annihilation and rearrangement of dislocations and substructures at high strain rates. The LAGBs were progressively transformed into HAGBs because of the accumulation of dislocations. This result was consistent with the observed increase in the orientation angle fraction from 30° to 60° [52]. The low strain rate allowed the samples to accumulate energy and annihilate dislocations continuously with sufficient time, which contributed to the growth of the recrystallized grains. As a result, the size of the recrystallized grains in the compressed steel specimens increased with a decrease in the strain rate.

The dislocations generated by the deformations that were tangled with each other impeded the further deformation of the naval steel. Subsequently, a surge in the stress was observed in the early stages of deformation. Meanwhile, the surge in dislocations gradually aggravated

DRV. Notably, austenite has a low stacking fault energy, which favors the recrystallization over the cross-slip mechanism [53]. Therefore, DRX began once the dislocation density in the naval steel accumulated to a certain extent. With the intensification of DRV and the occurrence of DRX, the consumption of dislocations gradually caught up with their generation, which eventually gave rise to a steady flow stress in the later stages of deformation. In addition, the increase in temperature can speed up DRV and DRX, which explains the observed decrease in the flow stress of this naval steel with an increase in the deformation temperature.

3.7 Processing map

Based on the dynamic materials model (DMM), the strain rate sensitivity (m) map and the processing map at $\varepsilon = 0.6$ were developed to optimize the thermal deformation parameters and control the microstructural evolution (Fig. 11). The processing map was formed by superimposing the instability map on the power dissipation map. According to Prasad's theory, the instability map and power dissipation map are representations of the variations in power dissipation efficiency (η) and instability parameter (ξ), respectively, as functions of temperature and strain rate. η represents the proportion of energy used for the microstructural evolution during thermal deformation,
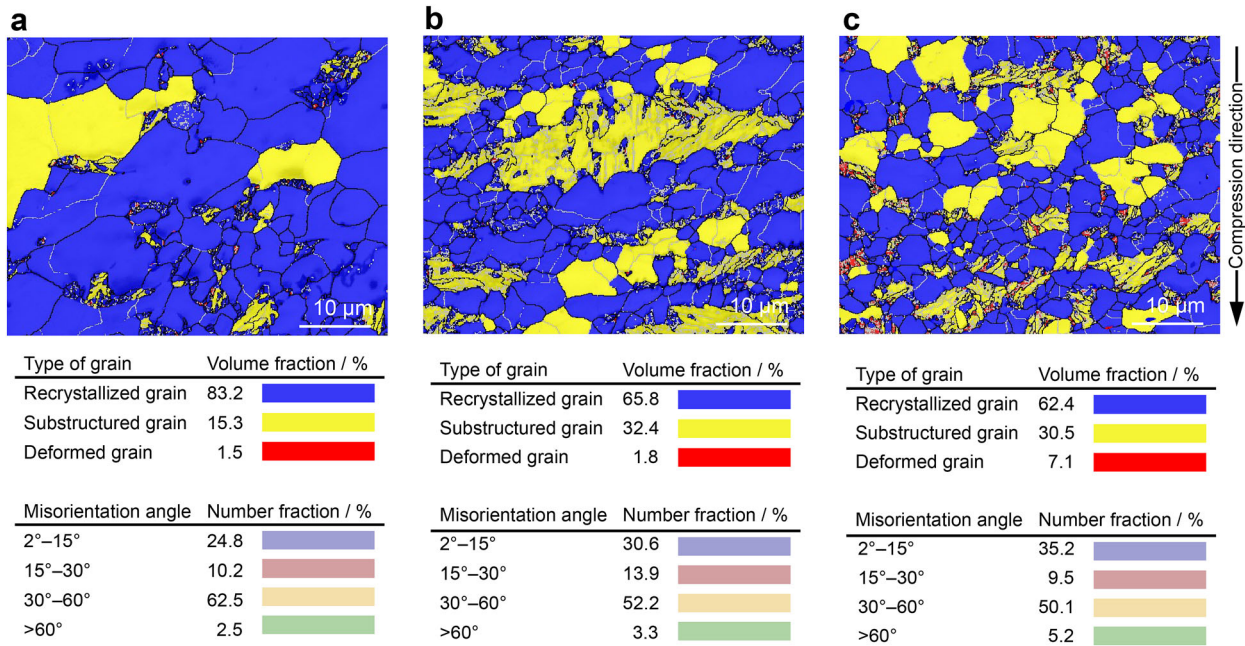
Fig. 10 Grain orientation spread maps, volume fraction of grains, number fraction of misorientation angle of naval steel samples compressed under different conditions: **a** 1023 K, 0.0005 s^{-1}; **b** 1023 K, 0.0050 s^{-1}; **c** 1023 K, 0.0100 s^{-1}
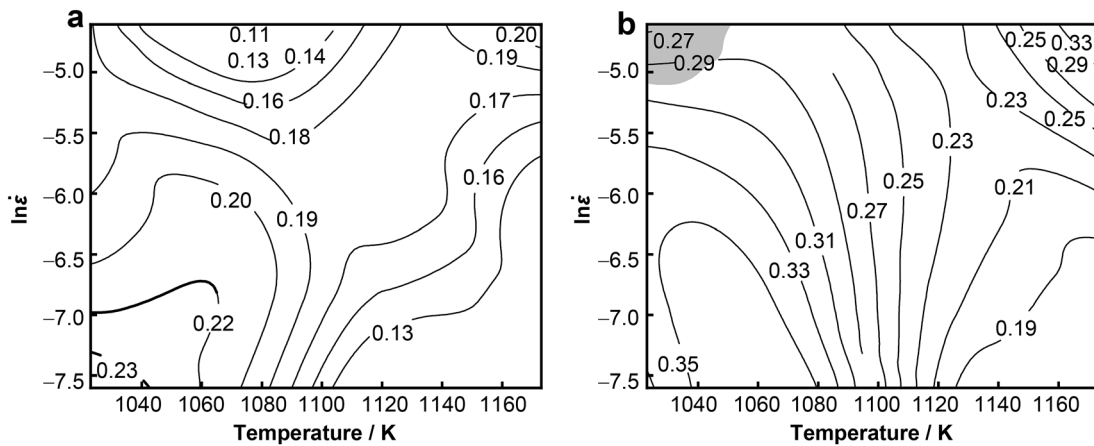

Fig. 11 **a** Strain rate sensitivity and **b** processing maps of steel at $\varepsilon = 0.6$

while ξ is used to assess the occurrence of rheological instabilities, including adiabatic shear bands, mechanical twinning, flow rotations, and flow localization, during deformation. These two parameters are given by Eqs. (19, 20) [54, 55]:

$$\eta = \frac{2m}{m+1} \tag{19}$$

$$\xi(\dot{\varepsilon}) = \frac{\partial \ln\left[\frac{m}{m+1}\right]}{\partial \ln \dot{\varepsilon}} + m < 0 \tag{20}$$

where m is the strain rate sensitivity of the material. It is defined by:

$$m = \frac{\partial(\ln \sigma)}{\partial(\ln \dot{\varepsilon})} \tag{21}$$

The shaded area in Fig. 11b is the area where ξ is less than 0. This corresponds to the instability region. Furthermore, this indicates that the thermal working of the naval steel at 1023–1073 K and 0.005–0.010 s^{-1} must be avoided. For optimal workability, regions with higher m and higher η are preferred [9, 55]. When the naval steel samples were deformed at a higher strain rate and lower temperature or at lower strain rate and higher temperature, m and η tend to be higher. Additionally, the processing efficiency must also be considered; thus, for the new steel,

the optimal thermal working parameters are in the temperature range of 1140–1173 K and strain rate range of 0.005–0.010 s^{-1}.

4 Conclusion

An SCAC model and an optimized BP-ANN model of a Cr-Mn-Si-Ni alloyed naval steel were established from the thermal compression experimental data obtained at different strain rates (0.0005–0.0100 s^{-1}) and temperatures (1023–1173 K). The optimized BP-ANN model exhibited more effective and accurate performance on predicting thermal forming behavior of Cr-Mn-Si-Ni alloyed naval steel comparing with the SCAC model. In addition, the processing map and the strain rate sensitivity map of the Cr-Mn-Si-Ni alloyed naval steel were provided. The optimized BP-ANN model exhibited more effective and accurate performance in predicting the thermal forming behavior of the Cr-Mn-Si-Ni alloyed naval steel than the SCAC model. During thermoplastic deformation, the dynamic recrystallization of Cr-Mn-Si-Ni alloyed naval steel can be improved by increasing the deformation temperature or decreasing the strain rate. At higher strain rates, microstructures with finer recrystallized grains were obtained after thermoplastic deformation.

Declarations

Conflict of interests The authors declare that they have no conflict of interest.

References

[1] Zhang JL, Jiang P, Zhu ZL, Chen Q, Zhou J, Meng Y. Tensile properties and strain hardening mechanism of Cr-Mn-Si-Ni alloyed ultra-strength steel at different temperatures and strain rates. J Alloy Compd. 2020;842:155856.

[2] Wang HP, Sun L, Shi J, Liu C, Jiang M, Zhang C. Inclusions and solidification structures of high pure ferritic stainless steels dual stabilized by niobium and titanium. Rare Met. 2014;33(6):761.

[3] Gheorghies C, Palaghian L, Baicean S, Buciumeanu M, Ciortan S. Fatigue behaviour of naval steel under seawater environmental and variable loading conditions. J Iron Steel Res Int. 2011;18:64.

[4] Benea L, Mardare L, Simionescu N. Anticorrosion performances of modified polymeric coatings on E32 naval steel in sea water. Prog Org Coat. 2018;123:120.

[5] Chen X, Qiu L, Tang H, Luo X, Zuo L, Wang Z, Wang Y. Effect of nanoparticles formed in liquid melt on microstructure and mechanical property of high strength naval steel. J Mater Process Technol. 2015;222:224.

[6] Yu X, Caron JL, Babu SS, Lippold JC, Dieter Isheim D, Seidman DN. Characterization of microstructural strengthening in the heat-affected zone of a blast-resistant naval steel. Acta Mater. 2010;58:5596.

[7] Shahriari B, Vafaei R, Sharifi EM, Farmanesh K. Modeling deformation flow curves and dynamic recrystallization of BA-160 steel during hot compression. Metals Mater Int. 2018;24(5):955.

[8] Abed FH. Constitutive modeling of the mechanical behavior of high strength ferritic steels for static and dynamic applications. Mech Time-Depend Mater. 2010;14(4):329.

[9] Dandekar TR, Khatirkar RK, Gupta A, Bibhanshu N, Bhadauria A, Suwas S. Strain rate sensitivity behaviour of Fe-21Cr-1.5Ni-5Mn alloy and its constitutive modelling. Mater Chem Phys. 2021;271:124948.

[10] Ashtiani HRR, Parsa MH, Bisadi H. Constitutive equations for elevated temperature flow behavior of commercial purity aluminum. Mater Sci Eng A. 2012;545:61.

[11] Chen G, Fu G, Lin S, Cheng C, Yan W, Chen H. Simulation of flow of aluminum alloy 3003 under hot compressive deformation. Metal Sci Heat Treat. 2013;54(11–12):623.

[12] Yang S, Li H, Luo J, Liu Y, Li M. Prediction model for flow stress during isothermal compression in α + β phase field of TC4 alloy. Rare Met. 2018;37(5):369.

[13] Lin YC, Xia YC, Chen XM, Chen MS. Constitutive descriptions for hot compressed 2124–T851 aluminum alloy over a wide range of temperature and strain rate. Comput Mater Sci. 2010;50(1):227.

[14] Li HY, Li YH, Wang XF, Liu JJ, Wu Y. A comparative study on modified Johnson Cook, modified Zerilli-Armstrong and Arrhenius-type constitutive models to predict the hot deformation behavior in 28CrMnMoV steel. Mater Des. 2013;49:493.

[15] Kim JH, Kim SK, Lee CS, Kim MH, Lee JM. A constitutive equation for predicting the material nonlinear behavior of AISI 316L, 321, and 347 stainless steel under low-temperature conditions. Int J Mech Sci. 2014;87:218.

[16] Niu LQ, Cao M, Liang ZL, Han B, Zhang Q. A modified Johnson-Cook model considering strain softening of A356 alloy. Mater Sci Eng A. 2020;789:10.

[17] Han Y, Qiao GJ, Sun JP, Zou DN. A comparative study on constitutive relationship of as-cast 904L austenitic stainless steel during hot deformation based on Arrhenius-type and artificial neural network models. Comput Mater Sci. 2013;67:93.

[18] Ashtiani HRR, Shahsavari P. A comparative study on the phenomenological and artificial neural network models to predict hot deformation behavior of AlCuMgPb alloy. J Alloy Compd. 2016;687:263.

[19] Tao ZJ, Yang H, Li H, Ma J, Gao P. Constitutive modeling of compression behavior of TC4 tube based on modified Arrhenius and artificial neural network models. Rare Met. 2015;35(2):162.

[20] Gupta AK, Anirudh VK, Singh SK. Constitutive models to predict flow stress in austenitic stainless steel 316 at elevated temperatures. Mater Des. 2013;43:410.

[21] Zerilli FJ, Armstrong RW. Dislocation-mechanics-based constitutive relations for material dynamics calculations. J Appl Phys. 1987;61(5):1816.

[22] Jia Z, Gao Z, Ji J, Liu D, Guo T, Ding Y. High-temperature deformation behavior and processing map of the as-cast Inconel 625 alloy. Rare Met. 2021;40(8):2083.

[23] Jiao L, Li M. Modeling of grain size in isothermal compression of Ti-6Al-4V alloy using fuzzy neural network. Rare Met. 2011;30(6):555.

[24] Li HY, Wang XF, Wei DD, Hu JD, Li YH. A comparative study on modified Zerilli-Armstrong, Arrhenius-type and artificial

neural network models to predict high-temperature deformation behavior in T24 steel. Mater Sci Eng A. 2012;536:216.

[25] Sabokpa O, Zarei-Hanzaki A, Abedi HR, Haghdadi N. Artificial neural network modeling to predict the high temperature flow behavior of an AZ81 magnesium alloy. Mater Des. 2012;39:390.

[26] Quan GZ, Pu SA, Zhan ZY, Zou ZY, Liu YY, Xia YF. Modelling of the hot flow behaviors for Ti-13Nb-13Zr alloy by BP-ANN model and its application. Int J Precis Eng Manuf. 2015;16(10):2129.

[27] Maati A, Tabourot L, Balland P, Ouakdi EH, Belaid S. A novel constitutive modelling for spring back prediction in sheet metal forming processes. In: Proceedings of the 6th Algerian Congress of Mechanics. Constantine; 2017.39.

[28] Oliveira SA, Savi MA, Zouain N. A three-dimensional description of shape memory alloy thermomechanical behavior including plasticity. J Braz Soc Mech Sci Eng. 2016;38(5):1451.

[29] Ashrafian MM, Kordkheili SAH. A novel phenomenological constitutive model for Ti-6Al-4V at high temperature conditions and quasi-static strain rates. Proceedings of the Institution of Mechanical Engineers, Part G. J Aerosp Eng. 2021;235(13):1831.

[30] Huang CQ, Jia XD, Zhang ZW. A modified back propagation artificial neural network model based on genetic algorithm to predict the flow behavior of 5754 aluminum alloy. Materials. 2018;11(5):15.

[31] Wan P, Zou H, Wang KL, Zhao ZZ. Research on hot deformation behavior of Zr-4 alloy based on PSO-BP artificial neural network. J Alloy Compd. 2020;826:9.

[32] Murugesan M, Sajjad M, Jung DW. Hybrid machine learning optimization approach to predict hot deformation behavior of medium carbon steel material. Metals. 2019;9(12):19.

[33] Lou Y, Wu WH, Li LX. Inverse identification of the dynamic recrystallization parameters for AZ31 magnesium alloy using BP neural network. J Mater Eng Perform. 2012;21(7):1133.

[34] Zhao D. Temperature correction in compression tests. J Mater Process Technol. 1993;36:467.

[35] Ke B, Ye LY, Tang JG, Zhang Y, Liu SD, Lin HQ, Dong Y, Liu XD. Hot deformation behavior and 3D processing maps of AA7020 aluminum alloy. J Alloy Compd. 2020;845:156113.

[36] Zhu F, Xiong W, Li X, Chen J. A new flow stress model based on Arrhenius equation to track hardening and softening behaviors of Ti6Al4V alloy. Rare Met. 2018;37(12):1035.

[37] Mostafaei MA, Kazeminezhad M. Hot deformation behavior of hot extruded Al-6Mg alloy. Mater Sci Eng A. 2012;535:216.

[38] Ebrahimi R, Najafizadeh A. A new method for evaluation of friction in bulk metal forming. J Mater Process Technol. 2004;152:136–43.

[39] Liang XP, Liu Y, Li HZ, Zhou CX, Xu GF. Constitutive relationship for high temperature deformation of powder metallurgy Ti-47Al-2Cr-2Nb-0.2W alloy. Mater Des. 2012;37:40.

[40] Wang WT, Guo XZ, Huang B, Tao J, Li HG, Pei WJ. The flow behaviors of CLAM steel at high temperature. Mater Sci Eng A. 2014;599:134.

[41] X. Zhou, X. Liu, Hot forming, behavior and flow stress model of steel 50A1300, In: Proceedings of the 2nd International Conference on Advances in Materials and Manufacturing Processes. Guilin; 2012.418.

[42] Xiao X, Liu GQ, Hu BF, Zheng X, Wang LN, Chen SJ, Ullah A. A comparative study on Arrhenius-type constitutive equations and artificial neural network model to predict high-temperature deformation behaviour in 12Cr3WV steel. Comput Mater Sci. 2012;62:227.

[43] Haghdadi N, Zarei-Hanzaki A, Khalesian AR, Abedi HR. Artificial neural network modeling to predict the hot deformation behavior of an A356 aluminum alloy. Mater Des. 2013;49:386.

[44] Li HY, Wei DD, Li YH, Wang XF. Application of artificial neural network and constitutive equations to describe the hot compressive behavior of 28CrMnMoV steel. Mater Des. 2012;35:557.

[45] Ozerdem MS, Kolukisa S. Artificial neural network approach to predict the mechanical properties of Cu-Sn-Pb-Zn-Ni cast alloys. Mater Des. 2009;30(3):764.

[46] Liu HD, Tang AT, Pan FS, Zuo RL, Wang LY. A model on the correlation between composition and mechanical properties of Mg-Al-Zn alloys by using artificial neural network. In: Proceedings of International Conference on Magnesium—Science, Technology and Applications. Beijing; 2005.488.

[47] Li P, Shan DB, Xue KM, Lu Y, Xu Y. Prediction of flow stress of Ti-15-3 alloy with artificial neural network. Trans Nonferr Metal Soc. 2001;11(1):95.

[48] Yang QY, Xiang S, Tan YB, Liu WC, Zhao F. Constitutive modeling for high-temperature flow behaviour of 47Zr-45Ti-5Al-3V alloy. Chin J Rare Met. 2020;44(8):816.

[49] Srinivasulu S, Jain A. Microstructure quantification of Cu–4.7Sn alloys prepared by two-phase zone continuous casting and a BP artificial neural network model for microstructure prediction. Rare Met. 2019;38(12):1124.

[50] Wang Q, Wu T, Sun DL, Lai J. Prediction of flow stress in Ti-6Al-4V alloy with hydrogen at high temperature using artificial neural network. In: Proceedings of the 5th International Conference on Processing and Manufacturing of Advanced Materials. Vancouver; 2007.539.

[51] Zhu Y, Zeng W, Sun Y, Feng F, Zhou Y. Artificial neural network approach to predict the flow stress in the isothermal compression of as-cast TC21 titanium alloy. Comput Mater Sci. 2011;50(5):1785.

[52] Wu H, Li Q, Xu B, Liu H, Shu G, Liu W. Improvement in irradiation resistance of FeCu alloy by pre-deformation through introduction of dense point defect sinks. Rare Met. 2021;40(4):885.

[53] Kumar A, Gupta A, Khatirkar RK, Bibhanshu N, Suwas S. Strain rate sensitivity behaviour of a chrome-nickel austentic-ferritic stainless steel and its constitutive modelling. ISIJ Int. 2018;58(10):1840.

[54] Li HJ, Yu Y, Song XY, Ye WJ, Hui SX. Thermal deformation behavior and processing map of a new type of Ti-6554 alloy. Chin J Rare Met. 2020;44(5):462.

[55] Sun Y, Wan Z, Hu L, Ren J. Characterization of hot processing parameters of powder metallurgy TiAl-based alloy based on the activation energy map and processing map. Mater Des. 2015;86:922.